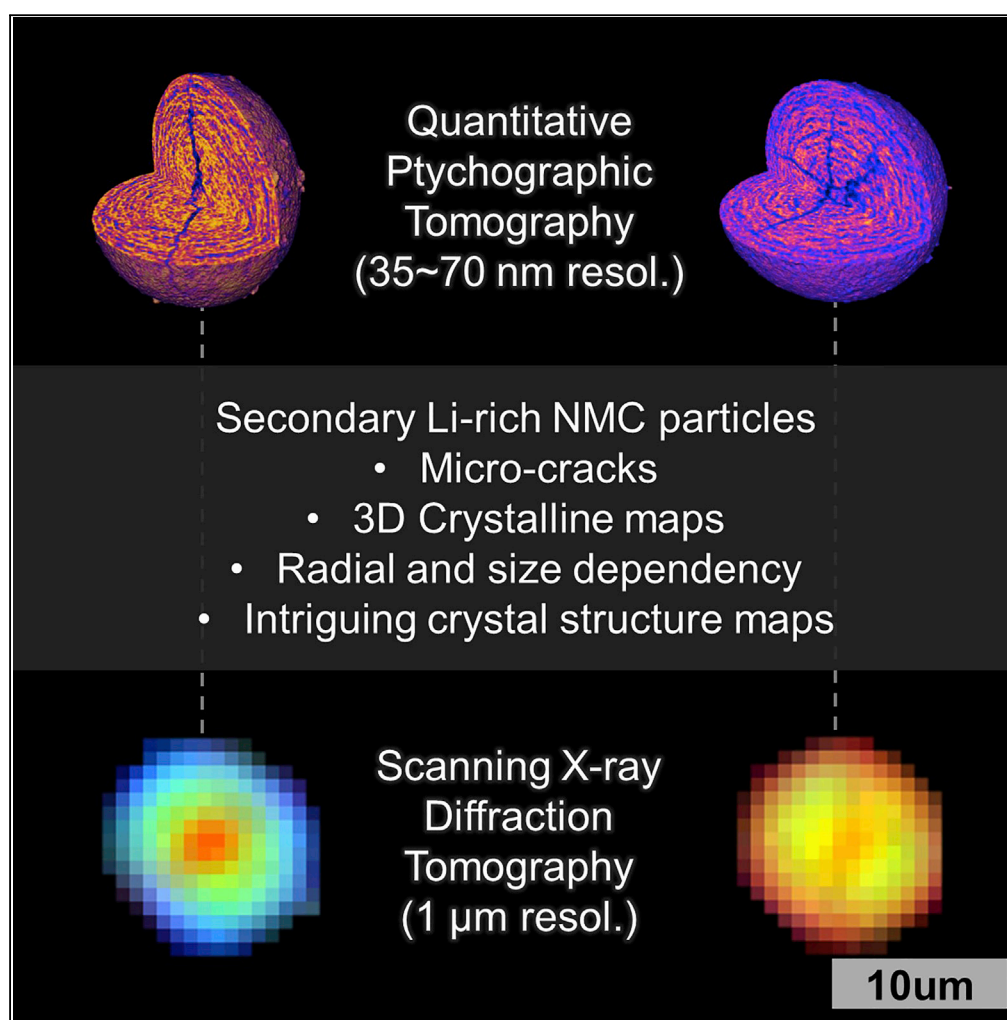**Article**

Correlated X-Ray 3D Ptychography and Diffraction Microscopy Visualize Links between Morphology and Crystal Structure of Lithium-Rich Cathode Materials

Esther H.R. Tsai, Juliette Billaud, Dario F. Sanchez, ..., Daniel Grolimund, Claire Villevieille, Manuel Guizar-Sicairos

etsai@bnl.gov (E.H.R.T.)
manuel.guizar-sicairos@psi.ch (M.G.-S.)

HIGHLIGHTS

Correlative ptychographic tomography with 35 nm resolution and diffraction tomography

3D micro-cracks in secondary Li-rich NMC particles correlated with crystal lattice

Radial and secondary-particle-size-dependent material degradation

Intriguing core-shell structure observed in 3D crystalline maps

Article

Correlated X-Ray 3D Ptychography and Diffraction Microscopy Visualize Links between Morphology and Crystal Structure of Lithium-Rich Cathode Materials

Esther H.R. Tsai,[1,3,5,6,*] Juliette Billaud,[2,5] Dario F. Sanchez,[1] Johannes Ihli,[1,4] Michal Odstrčil,[1] Mirko Holler,[1] Daniel Grolimund,[1] Claire Villevieille,[2] and Manuel Guizar-Sicairos[1,*]

SUMMARY

The search for higher performance, improved safety, and lifetime of lithium-ion batteries relies on the understanding of degradation mechanisms. Complementary to methods and studies on primary particles or crystalline structure on bulk materials, here we use spatially correlated ptychographic X-ray computed nanotomography with a 35 nm resolution and scanning X-ray diffraction microscopy with 1 μm resolution to visualize in 3D the hidden morphological and structural degradation processes in individual secondary particles of lithium-rich nickel, cobalt, and manganese oxides. From comparative examination of pristine and cycled particles, we suggest that morphological degradation could have radial dependency and secondary particle size dependency. The same particles were examined to correlate the degradation to crystallinity, which shows surprising core-shell structures. This study reveals the inner 3D structure of the secondary particles while opening up questions on the unexpected crystalline structural distributions, which could offer clues for future studies on this promising cathode material for lithium-ion batteries.

INTRODUCTION

Lithium-rich nickel, manganese, and cobalt oxides (Li-rich NMC) offer considerable performance advantages over industry standards for cathode materials used in lithium-ion batteries (Thackeray et al., 2007; Rozier and Tarascon, 2015; Wang et al., 2016; Pimenta et al., 2017; Etacheri et al., 2011; Schipper et al., 2017). These advantages include a high average working potential, ca. 3.8 V versus Li^+/Li, and a specific charge of over 250 mAh/g, which corresponds to an energy density of over 900 Wh/kg, higher than that of $LiFePO_4$ or $LiCoO_2$ materials. However, the high operating voltage, first cycle activation, repeated lithiation/delithiation phenomenon, and the anionic redox processes result in structural and chemical degradation, impeding their commercialization. Degradation processes upon cycling and their prevention are thus under extensive investigation (Liu et al., 2017; Croy et al., 2016; Klein et al., 2015; Boulet-Roblin et al., 2015; Watanabe et al., 2014; Amalraj et al., 2013). This includes examination of alternative synthesis procedures, protective coatings or surface treatments, dopings, or modification of the cycling protocol. Commonly, studies examine processes on the primary particle or the bulk level (Kang et al., 2007; Lim et al., 2009; Li et al., 2013; Mohanty et al., 2014; Sasakawa et al., 2015; Gilbert et al., 2017; Kuppan et al., 2017). It was identified that electrochemical activation of the material occurring at the first delithiation is accompanied by oxygen loss from the crystal structure (Lu and Dahn, 2002; Tran et al., 2008; Mu et al., 2018). Continued cycling was shown to not only promote the formation of a new unstable spinel-like phase growing from the surface in the direction of the core but also highlighted the passivation of electrode surfaces by electrolyte decomposition and the degradation of the active material itself by means of transition metal leaching and lithium loss (Gu et al., 2013; Lin et al., 2014; Mukhopadhyay and Sheldon, 2014; Yan et al., 2017; Strehle et al., 2017; Zhan et al., 2018; Tan et al., 2014).

These predominantly chemistry-driven degradation processes are accompanied by well-known but less studied morphological degradation processes in particular on the single secondary particle level (Lee et al., 2014; Yang et al., 2014; Chen et al., 2016; Sun and Manthiram, 2017; Kondrakov et al., 2017; Ryu et al., 2018; Ko et al., 2019; Gent et al., 2016). The Li-rich NMC particles studied in this work are in the form of micron-sized spheres composed of thousands of tightly packed primary particles, 50 to 100 nm

[1]Swiss Light Source, Paul Scherrer Institut (PSI), 5232 Villigen, Switzerland

[2]Electrochemistry Laboratory, Paul Scherer Institut (PSI), 5232 Villigen, Switzerland

[3]Present address: Center for Functional Nanomaterials, Brookhaven National Laboratory, Upton, New York 11973, USA

[4]Present address: Department of Materials, University of Oxford, Oxford OX2 6HT, UK

[5]These authors contributed equally

[6]Lead Contact

*Correspondence: etsai@bnl.gov (E.H.R.T.), manuel.guizar-sicairos@psi.ch (M.G.-S.)

https://doi.org/10.1016/j.isci.2018.12.028

in diameter, and possess a synthesis-inherent onion-like structure. During cycling, lithium is extracted from and reinserted into the interlayer, generating stress along the c-axis of the oxide by up to 2% changes (Yoon et al., 2006). Although the inner porosity of such compounds can accommodate part of these volume changes, the changes can eventually generate a significant stress that leads to the formation of cracks on the secondary particles, i.e., micro-cracks, and in turn pulverization, ultimately resulting in battery failures due to the loss of electronic contact.

The high resolution provided by methods such as electron microscopy or atomic force microscopy (Etacheri et al., 2011; Schipper et al., 2017) allows for studying the surface of the material and the primary particles. Complementary to such studies, here we show a study on the morphological and crystalline structural changes for the secondary particles, offering insight into the battery material from a different perspective on a different scale. Through spatially correlated ptychographic X-ray computed tomography (PXCT) and scanning X-ray diffraction microscopy (SXDM), we visualize these changes in 3D within individual secondary particles. Li-rich NMC secondary particles were examined in their pristine state, after the first delithiation, and after long-term cycling, in which the cells were stopped after full lithiation. All particles in this work refer to secondary particles unless stated otherwise. PXCT (Dierolf et al., 2010; Holler et al., 2014) is a lensless imaging technique that provides quantitative electron density tomograms of extended system at spatial resolution levels hardly achievable by common X-ray microscopic techniques, here 35 to 70 nm. Morphological changes were observed in aged particles through PXCT and correlated with the expansion of the unit cell volume through subsequent SXDM measurements with 1 µm resolution on the same particles. X-ray fluorescence (XRF) spectra were also collected with the SXDM measurements simultaneously.

RESULTS AND DISCUSSION

Electrochemical Performance and Morphological Characterization

The studied Li-rich NMC particles were obtained from a commercial source (see Transparent Methods) with a composition of $Li_y(Ni_{0.19}Mn_{0.54}Co_{0.1})O_{2-x}$, where $y = 1.17$ and $x = 0$ in the pristine stage and, after the first delithiation, $y \approx 0.2$ associated with the activation of the Li_2MnO_3 phase (Johnson et al., 2004) and $x > 0$ accounting for the oxygen loss. This type of material typically loses around 6% oxygen after the first cycle (Tran et al., 2008). Given the gradual structural changes, transition metal leaching, and electrolyte decomposition at potentials above 4.3 V versus Li^+/Li (Tasaki et al., 2009; Guéguen et al., 2016), fewer lithium ions are reversibly exchanged upon further cycling, giving $y \approx 0.7$ for long-term cycled particles. Instead of observing these established phenomena directly, this study aims to determine their effects on the morphological and crystalline structural maps.

Scanning electron micrographs in Figure 1 provide a general picture of the secondary particles. Figure 1A shows the pristine particles; Figure 1B shows the particles once delithiated, i.e., after activation; and Figure 1C shows the particles after long-term cycling, i.e., after 85 charge-discharge cycles at a rate of C/10. These secondary particles are 5–20 µm in diameter. Pristine particles exhibit a relatively spherical and regular surface. Among cycled particles, some particles showed faint cracks on the surface and some revealed the internal onion-like structure composed of alternating pores and primary particles. The electrochemical performance shown in Figure 1D revealed a roughly 20% loss of specific charge after the first cycle and a further decrease after long-term cycling. Figure S1 shows the first cycle activation of the NMC particles. The performance decay implies particle degradation; however, many aged particles in Figures 1B and 1C appeared to be intact when observed through scanning electron microscope. With complementary tomographic methods, the interior 3D structures can be revealed to offer better understanding and control of the material.

Three-Dimensional Electron Density Maps by Ptychographic X-Ray Computed Nanotomography

For the series of PXCT and SXDM measurements, the Li-rich NMC particles were transferred into tapered glass capillaries mounted on tomography pins. Pristine, delithiated, and cycled particles were prepared and handled in inert atmosphere, and the capillaries were sealed airtight. Pytchography is a high-resolution lensless coherent diffractive imaging method (Rodenburg et al., 2007; Faulkner and Rodenburg, 2004), which, when combined with tomography, offers quantitative electron density and absorption tomograms with nanoscopic resolution when incident X-ray energies are away from the absorption edge (Dierolf et al., 2010; Holler et al., 2014, 2017). PXCT experiments (Holler et al., 2012) were performed at the cSAXS beamline (X12SA) of the Swiss Light Source, Paul Scherrer Institut, Switzerland. Experimental details are provided
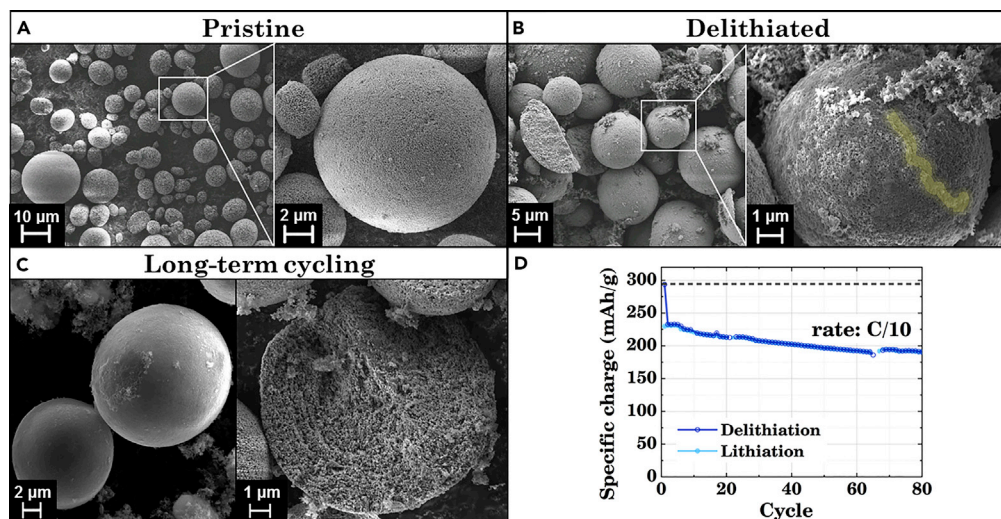
Figure 1. Surface Geometry and Electrochemical Performance of Li-rich NMC

(A–C) Scanning electron micrographs of (A) pristine NMC particles, (B) after first delithiation, and (C) after long-term cycling. Primary particles consist of 50- to 100-nm grains that aggregate to form the secondary particles with diameters of around 5 to 20 μm. A crack on the surface is highlighted in yellow in (B), although the spatial extent of the crack is unknown. Onion-like layered structures are observed from broken particles in (C).

(D) The evolution of the specific charge upon cycling at C/10 after the first cycle activation at C/20. The dashed line gives the specific charge obtained after the first cycle.

See also Figure S1 for the first cycle activation.

in the Transparent Methods. Multiple high-resolution ptychographic tomograms were collected to account for the varying secondary particle size. In total, 7 tomograms of pristine, 5 tomograms of delithiated, and 12 tomograms of long-term cycled particles were acquired. An overview of the acquired PXCT tomograms is given in Figure S2, where the aforementioned onion-like structure is clearly visible. Spatial resolutions were determined by Fourier shell correlation (Van Heel and Schatz, 2005) and range from 35 to 70 nm.

Orthoslices and volume renderings of representative electron density tomograms obtained through PXCT are shown in Figure 2. The measured electron density (Diaz et al., 2012), n_e, can be related to the material composition through $n_e = (\rho Z N_A)/A$, where ρ is the mass density, Z is the number of electrons of the average molecule in the voxel, N_A is the Avogadro's number, and A is the molar mass. The expected theoretical value of the NMC is roughly 1 $e/\text{Å}^3$ for ρ = 3.6 g/cm^3. Owing to the partial volume effects, i.e., the intermixture of unresolved pores with NMC material, measured values that are lower than the theoretical intrinsically indicate the porosity.

Pristine particles display alternating concentric layers of rather uniform thickness and uniform electron density from the core to the edge of the particle, as observed in Figure 2A. After the first charge, i.e., on delithiated particles, we observe an overall widening of the pores as well as the first signs of crack formation, as shown in Figure 2B. These internal morphological changes continue upon prolonged cycling with particles decreasing in electron density, cracking, or fracturing entirely, as observed in Figures 2C–2E. A video of the 3D rendering for the particle in Figure 2D is given in Video S1. Particle exteriors are given in grayscale electron density in Figures 2F–2H with cracks highlighted. Their corresponding volume renderings on the first row show that major fracturing begins at the core and in some cases extends to the surface. We have complemented our observation in regard to morphology change using lower resolution measurements with near-field ptychography on the same ptychography setup with a modified reconstruction algorithm (Odstrčil et al., 2018), showing several particles with cracks from the core, as shown in Figure S3.

Figures 2I–2M show the cross-sections of each particle, giving the pore networks obtained through image segmentation (see Transparent Methods). For the upper right half of each subfigure, the electron density is shown as a reference to show the accuracy of the segmentation. The pore size distribution ranges from a few nanometers to around 200 nm, calculated based on the segmentation. The corresponding histograms
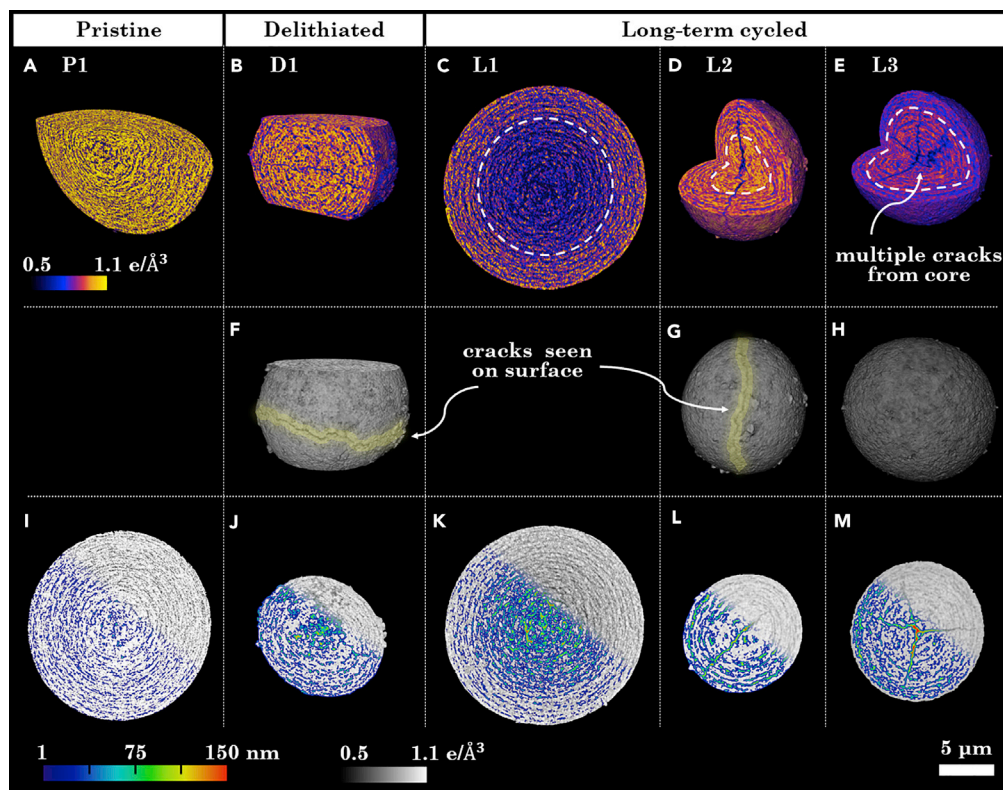
Figure 2. Ptychographic X-ray Computed Tomography (PXCT) for Li-rich NMC Secondary Particles

(A–E) Volume rendering of (A) pristine, (B) delithiated, and (C–E) cycled particles. Cracks originated from the particle cores can be seen in (B), (D), and (E).

(F–H) Exterior of cracked particles. Surface cracks are seen on particles in (F) and (G) while particle in (H) appears to be intact from the surface. Common to all subfigures is a linear color scale ranging from 0.5 to 1.1 $e/\text{Å}^3$ for the electron density.

(I–M) Cross-sections of the particles. The lower left half of each image shows the pore diameter maps given in color scale ranging from 1 to 150 nm. The upper right parts give the electron density in grayscale. Pristine particle in (I) has in general smaller pores, seen as dark blue, compared to the larger pores in particles (J-M), seen as teal or orange.

See also Figure S2 for high-resolution tomograms of all particles and Figure S3 for delithiated particles imaged with near-field ptychography.

of this distribution are given in Figure 3A, showing increases in both the number of pores and the pore diameter upon aging.

Alternatively, we also use a direct measure for the porosity without image segmentation as a way to circumvent the influence of partial volume effects and possible inaccuracy in segmentation by calculating the radially averaged electron density to compare particles, as shown in Figure 3B. The line plots were fitted quadratically and averaged over several tomograms with error bars indicating half of the standard deviation. Pristine particles display a relatively constant density from the surface to the core of around 0.95 $e/\text{Å}^3$, which approximates the expected Li-rich NMC electron density and thus indicates a low porosity. Delithiated particles possess an equally homogeneous electron density distribution at a lower averaged electron density of roughly 0.85 $e/\text{Å}^3$. Long-term cycled particles also show a lower averaged electron density compared with the pristine particle and, moreover, suggest a size dependency.

We categorize large secondary particles as those around or greater than 15 μm in diameter, and the rest are categorized as small secondary particles. Based on our collected data, we suggest that the extent of the damage is particle size dependent. As seen in Figures 2C–2E, large particles seem to be less affected by fracture mechanisms than the small particles. Moreover, an increase in pore frequency and size, i.e., material depletion is noticeable in the direction of the particle core for larger particles. This is shown quantitatively by the light violet curve in Figure 3B. For smaller cracked particles a higher porosity is observed
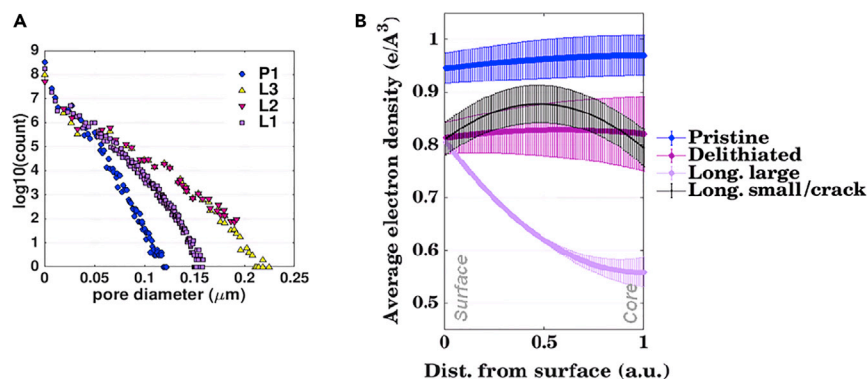
Figure 3. Pore Analysis for PXCT Tomograms

(A) The pore diameter distributions for particles shown in Figure 2, showing an increase in pore size and number upon activation and aging.

(B) Electron density with respect to normalized particle radius, reflecting the porosity distribution. Each curve was obtained by averaging over all particles in the category and the error bars indicate half of the standard deviation.

closer to the surface, shown by the black curve in Figure 3B. The dashed white lines in Figures 2C and 2E highlight the boundaries at which the electron density or porosity changes. The size dependency we observed here offers clues for the degradation mechanism.

The surface of secondary/primary particles with short diffusion pathways, such as those close to pores or diffusion highways, reacts first with the lithium ions during lithiation/delithiation, while the reaction front progresses toward the center of the secondary particle. Assuming the obedience of such surface diffusion model and that all secondary particles have a uniform porosity at their pristine stage regardless of diameter, repeated volume expansion/contraction of the primary particles can cause a strain differential inside the secondary particle whose magnitude is governed by, for example, the secondary particle diameter, material chemical composition and porosity, and cycling conditions. The strain differential due to expansion results in a tendency for a spherical particle to crack from the core to the surface once a critical strain value is surpassed (Kondrakov et al., 2017; Sun and Manthiram, 2017; Ryu et al., 2018; Ko et al., 2019; Christensen and Newman, 2006). This can lead to the observed difference in cracking behavior for different sizes of particles. The larger particles retain their structural integrity, although they display higher porosity at the core due to their size and longer diffusion pathways when compared with the smaller particles at a set cycling rate. Smaller secondary particles are subjected to an increased level of surface damage as they are cycled faster to completion and to a deeper extent because of the higher surface-area-to-volume ratio and shorter diffusion paths. Cracks also create more channels for electrolyte infiltration and interfaces for electrolyte decomposition. With this cracking mechanism in mind, we turned to X-ray diffraction microscopy to examine the crystallographic structure of the material and its correlation to the observed morphology.

Structural and Chemical Distribution within Particles at a 1 μm Resolution

We performed a series of SXDM measurements combined with XRF spectroscopy measurements on the same particles to infer how and if these morphological changes observed from PXCT results relate to changes in chemical composition and thus different extent of lithiation. Experiments were performed at the microXAS beamline of the Swiss Light Source, Paul Scherrer Institut, Switzerland. Through XRF tomography, a homogeneous distribution of Mn, Co, and Ni is observed for these same particles, as shown in Figure S4. However, SXDM measurements reveal unexpected findings.

Typically X-ray diffraction measurements are performed on bulk particles to obtain averaged X-ray diffractograms, e.g., Figure S5, whereas here we scanned samples with a 1-μm beam to probe each Li-rich NMC secondary particle individually. Diffraction maps highlighting the normalized integrated intensity of the selected (101), (104), and (003) Bragg peaks are given in Figure 4A in red, green, and blue, respectively. These selected peaks reflect the interlayer spacing where the Li ions are located, and they shift upon lithiation and delithiation (Mohanty et al., 2013). For visualization, the ratio of the intensity of these Bragg reflections is given in the form of a red-green-blue color map, in which each peak intensity is normalized with
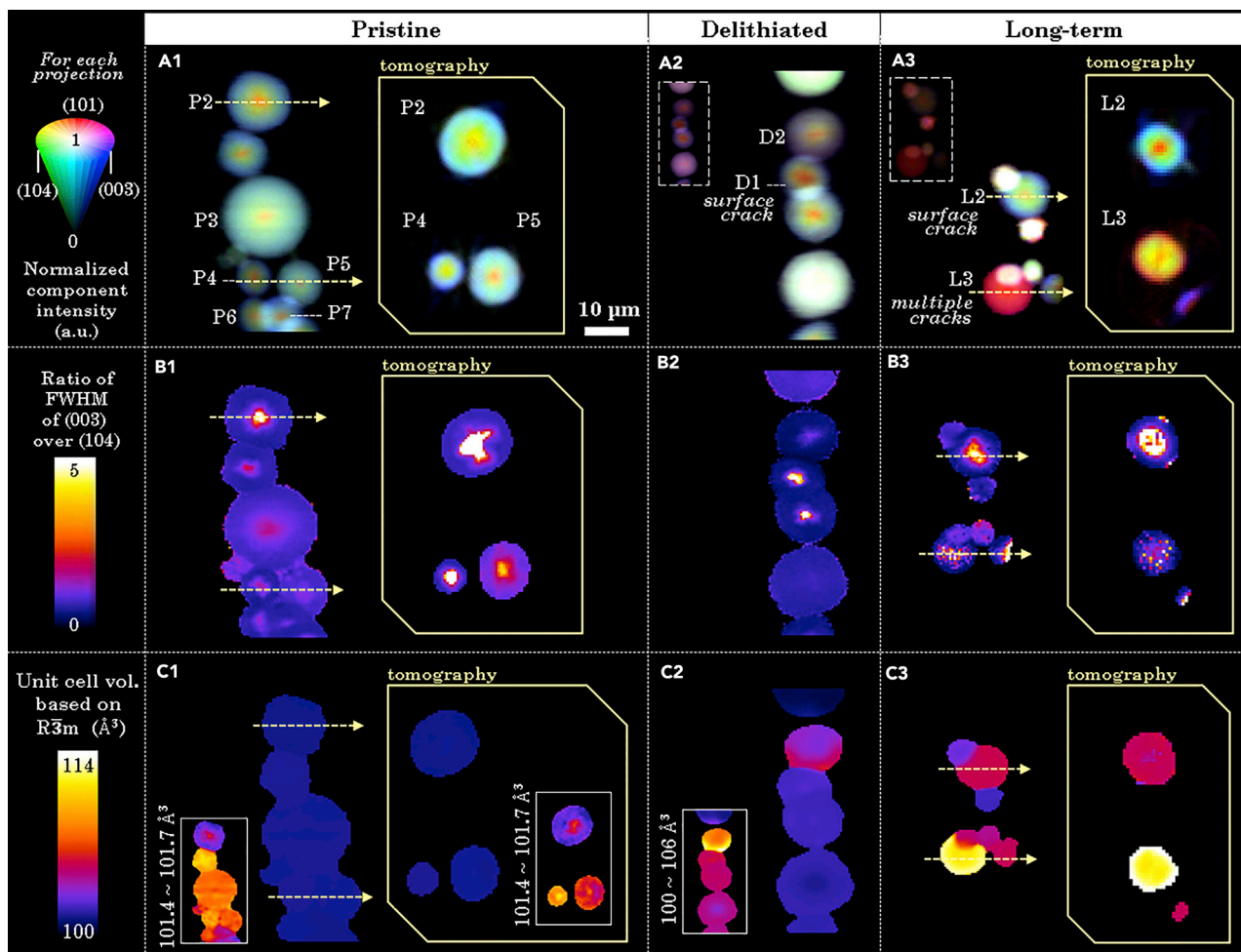
Figure 4. Scanning X-ray Diffraction Microscopy (SXDM) for Secondary NMC Particles

(A) X-ray diffraction intensity maps of (A1) the pristine, (A2) delithiated particles, and (A3) particles after long-term cycling. Each projection or tomogram gives the normalized intensity with the (101) Bragg reflection distribution map shown in red, (104) in green, and (003) in blue. Dashed lines in insets show the normalization with respect to pristine in (A1), showing a reduced crystallinity upon cycling.

(B) Ratio of the FWHM (003) peak over the FWHM (104) peak, showing a higher anisotropic disorder in some regions.

(C) Unit cell volume calculated based on the rhombohedral $R\bar{3}m$ model. Insets given with a different color scale show slight variation between particles within a projection. Comparison between (C1) and (C3) shows obvious increase of the unit cell volume for some particles. The pixel size is roughly 1 μm. The corresponding elemental distribution of Mn, Co, and Ni obtained from the XRF spectra is shown in Figure S4.

respect to its maximum in the projection. To compare between the particles at different stages, the dashed lines in insets in Figure 4A (A2 and A3) show the intensities normalized with respect to the corresponding peaks in the pristine projection. The reduced brightness from Figure 4A (A1) to the insets in Figure 4A (A2 and A3) reflects a reduced crystallinity upon cycling. Particles regardless of age and diameter possess an intriguing core-shell structure. A dominant (003) peak in blue is observed on the outermost shell, dominant (104) peak in green is seen on the inner shell, and dominant (101) peak in red is seen at the core. We attribute this core-shell crystal structure to a disorder in the structure and potentially lithium gradient from the shell to the core. With delithiation and prolonged cycling, the spatial extent of the core slightly increases and, in the case of some cracked particle, the shell is disappearing.

The ratio of the (003) and (104) reflects the cation intermixing and related structural disorder (Sasakawa et al., 2015; Fujii et al., 2007). Figure 4B (B1 to B3) gives the ratio of the full-width-half-maximum (FWHM) of the (003) peak over the FWHM of the (104) peak, showing in some regions a higher disorder, potentially attributed to less amount of Li ions in the lattice.
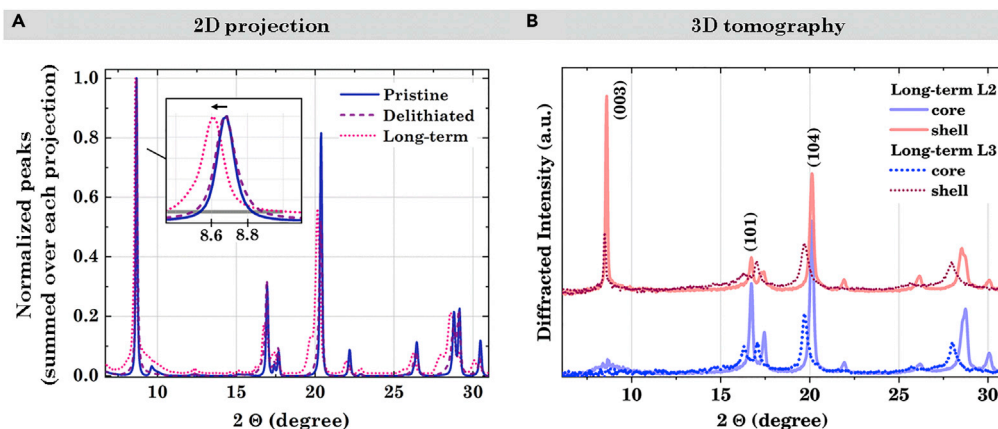
Figure 5. X-ray Diffraction Peaks in Projections and Voxels
(A) Averaged peaks for projections, showing shifting and broadening of the (003) peak upon aging, noted by the black arrow and the gray line, respectively.
(B) Typical single voxel (0.5 × 0.5 × 0.5 μm^3) powder diffraction patterns from the shell, i.e., near the particle surface, and the core of particles L2 and L3 retrieved through SXDM tomography. Typical X-ray diffractograms of bulk pristine and cycled NMC are given in Figure S5.

Although pristine NMC has a combination of rhombohedral and monoclinic phases, the rhombohedral model gives a relatively better fit to the data here compared with other models. The extrapolated interpretation presented here is an attempt to explain the surprising core-shell structure, inviting further investigation. Figure 4C (C1 to C3) gives the unit cell volume maps assuming the rhombohedral R$\bar{3}$m model, showing a volume expansion of 5% to 10%, compatible with the usually reported volumetric expansion upon cycling (Ates et al., 2013; Mohanty et al., 2013). Correlating this result with PXCT shows a relation between the extent of cracking with the degree of unit cell expansion. Multiple cracks near the core of L3 in Figure 2E correlate with reduced electron density and the most dramatic change in the crystal structure with over 10% volume expansion. Particles with a single crack extended to the surface show a lesser degree of changes. This type of crack formation leads to new exposed surface area that generates parasitic reactions that could possibly slow the aging of the crystal structure as some charge is consumed at each cycle to passivate the newly created surfaces.

Average peaks of projections in each state are given in Figure 5A, where prominent peaks bear high similarity with the X-ray diffractogram of bulk particles in Figure S5, giving validity to our measurements. Figure 5A also shows the shifting and broadening of the (003) peak, as expected for aged Li-rich NCM (Tran et al., 2006; Croy et al., 2013; Mohanty et al., 2013). The shifting is noted by the black arrow, and the broadening, by the gray line in the inset. Shown in Figure 5B is a comparison between typical single 0.5-μm-voxel powder diffraction patterns of particles L2 and L3, from their core and shell regions. A lower crystallinity is observed for the particle L3 in Figure 5B, and higher disorder along the *c* crystalline direction is observed in the core region for both these particles. This surprising core-shell structure deserves further investigation and could offer a different perspective for future studies.

Conclusions

Our examination of Li-rich NMC secondary particles revealed a series of morphological degradation processes on the secondary particle level that could complement current understandings of battery failure mechanisms. Acquired electron density tomograms of the spherical NMC particles with nanoscale resolution (35–70 nm) through PXCT revealed that the uniform onion-like layer-by-layer structure, common to most particles, changes upon going through a size-dependent aging mechanism. After long-term cycling, we observed that particles greater than 15 μm in diameter revealed an enhanced material depletion near the core, whereas smaller particles tend to be subjected to crack formation and depletion close to the surface. This size dependency gives insight into the aging mechanism and also draws attention to its possible influence on the performance. To better understand the degradation mechanism, we turned to SXDM with a 1 μm resolution to explore the relation between morphological and crystallographic change. A correlation between the spatial extent of the cracks and degree of unit cell volume expansion was observed. The SXDM results also present an intriguing spatially dependent crystal structure, seen as core shell, whose

extent changes upon aging. This core-shell structure is inferred from the intensity ratio of selected Bragg peaks. Aspects of the SXDM result that are different from typical observations on bulk NMC material could give a different perspective while inviting for further studies. Complementary to studies on the primary particles or on a bulk level, this work reveals in 3D the cathode material on a secondary particle level with regard to both its morphology and crystalline structure, a connection that could lead to a thorough fundamental understanding of the aging mechanism as well as present a method for studying battery materials in general.

Limitations of the Study

Particles were extracted from cells after cycling for imaging in this work, with resolution limited by the sample size and the experimental time. With ongoing instrumentation advances, future studies will seek fast high-resolution imaging of cells operando.

METHODS

All methods can be found in the accompanying Transparent Methods supplemental file.

SUPPLEMENTAL INFORMATION

Supplemental Information includes Transparent Methods, five figures, and one video and can be found with this article online at https://doi.org/10.1016/j.isci.2018.12.028.

AUTHOR CONTRIBUTIONS

E.H.R.T, J.B., and M.H. contributed to the sample preparation; E.H.R.T., M.H., M.G.S., J.I., D.F.S., J.B., M.O., D.G., and C.V. were involved in the measurements; E.H.R.T., D.F.S., and J.I. were responsible for the reconstruction and data analysis. All co-authors contributed to the discussion and interpretation of the results and the writing of this manuscript.

DECLARATION OF INTERESTS

The authors declare no competing interests.

REFERENCES

Amalraj, F., Talianker, M., Markovsky, B., Burlaka, L., Leifer, N., Goobes, G., Erickson, E.M., Haik, O., Grinblat, J., Zinigrad, E., et al. (2013). Studies of Li and Mn-rich $Li_x[MnNiCo]O_2$ electrodes: electrochemical performance, structure, and the effect of the aluminum fluoride coating. J. Electrochem. Soc. *160*, A2220–A2223.

Ates, M.N., Jia, Q., Shah, A., Busnaina, A., Mukerjee, S., and Abraham, K.M. (2013). Mitigation of layered to spinel conversion of a Li-rich layered metal oxide cathode material for Li-ion batteries. J. Electrochem. Soc. *161*, A290–A301.

Boulet-Roblin, L., Kazzi, M.E., Novak, P., and Villevieille, C. (2015). Surface/interface study on full xLi_2MnO_3 (1-x)$LiMO_2$ (M = Ni, Mn, Co)/ graphite cells. J. Electrochem. Soc. *162*, A1297–A1300.

Chen, C.J., Pang, W.K., Mori, T., Peterson, V.K., Sharma, N., Lee, P.H., Wu, S.h., Wang, C.C., Song, Y.F., and Liu, R.S. (2016). The origin of capacity fade in the $Li_2MnO_3·LiMO_2$ (M=Li, Ni, Co, Mn) microsphere positive electrode: an operando neutron diffraction and transmission X-ray microscopy study. J. Am. Chem. Soc. *138*, 8824–8833.

Christensen, J., and Newman, J. (2006). Stress generation and fracture in lithium insertion materials. J. Solid State Electrochem. *10*, 293–319.

Croy, J.R., Gallagher, K.G., Balasubramanian, M., Chen, Z., Ren, Y., Kim, D., Kang, S.H., Dees, D.W., and Thackeray, M.M. (2013). Examining hysteresis in composite xLi_2MnO_3 (1-x)$LiMO_2$ cathode structures. J. Phys. Chem. C *117*, 6525–6536.

Croy, J.R., Park, J.S., Shin, Y., Yonemoto, B.T., Balasubramanian, M., Long, B.R., Ren, Y., and Thackeray, M.M. (2016). Prospects for

spinel-stabilized, high-capacity lithium-ion battery cathodes. J. Power Sources 334, 213–220.

Diaz, A., Trtik, P., Guizar-Sicairos, M., Menzel, A., Thibault, P., and Bunk, O. (2012). Quantitative x-ray phase nanotomography. Phys. Rev. B 85, 020104.

Dierolf, M., Menzel, A., Thibault, P., Schneider, P., Kewish, C.M., Wepf, R., Bunk, O., and Pfeiffer, F. (2010). Ptychographic X-ray computed tomography at the nanoscale. Nature 467, 436–439.

Etacheri, V., Marom, R., Elazari, R., Salitra, G., and Aurbach, D. (2011). Challenges in the development of advanced Li-ion batteries: a review. Energy Environ. Sci. 4, 3243–3262.

Faulkner, H.M.L., and Rodenburg, J.M. (2004). Movable aperture lensless transmission microscopy: a novel phase retrieval algorithm. Phys. Rev. Lett. 93, 023903.

Fujii, Y., Miura, H., Suzuki, N., Shoji, T., and Nakayama, N. (2007). Structural and electrochemical properties of $LiNi_{1/3}Co_{1/3}Mn_{1/3}O_2$: calcination temperature dependence. J. Power Sources 171, 894–903.

Gent, W.E., Li, Y., Ahn, S., Lim, J., Liu, Y., Wise, A.M., Gopal, C.B., Mueller, D.N., Davis, R., Weker, J.N., et al. (2016). Persistent state-of-charge heterogeneity in relaxed, partially charged $Li_{1-x}Ni_{1/3}Coi_{1/3}Mni_{1/3}O_2$ secondary particles. Adv. Mater. 28, 6631–6638.

Gilbert, J.A., Shkrob, I.A., and Abraham, D.P. (2017). Transition metal dissolution, ion migration, electrocatalytic reduction and capacity loss in lithium-ion full cells. J. Electrochem. Soc. 164, A389–A399.

Gu, M., Belharouak, I., Zheng, J., Wu, H., Xiao, J., Genc, A., Amine, K., Thevuthasan, S., Baer, D.R., Zhang, J.G., et al. (2013). Formation of the spinel phase in the layered composite cathode used in Li-ion batteries. ACS Nano 7, 760–767.

Guéguen, A., Streich, D., He, M., Mendez, M., Chesneau, F.F., Novák, P., and Berg, E.J. (2016). Decomposition of $LiPF_6$ in high energy lithium-ion batteries studied with online electrochemical mass spectrometry. J. Electrochem. Soc. 163, A1095–A1100.

Holler, M., Diaz, A., Guizar-Sicairos, M., Karvinen, P., Färm, E., Härkönen, E., Ritala, M., Menzel, A., Raabe, J., and Bunk, O. (2014). X-ray ptychographic computed tomography at 16 nm isotropic 3D resolution. Sci. Rep. 4, 3857.

Holler, M., Guizar-Sicairos, M., Tsai, E.H.R., Dinapoli, R., Müller, E., Bunk, O., Raabe, J., and Aeppli, G. (2017). High-resolution non-destructive three-dimensional imaging of integrated circuits. Nature 543, 402–406.

Holler, M., Raabe, J., Diaz, A., Guizar-Sicairos, M., Quitmann, C., Menzel, A., and Bunk, O. (2012). An instrument for 3d x-ray nano-imaging. Rev. Sci. Instrum. 83, 073703.

Johnson, C., Kim, J., Lefief, C., Li, N., Vaughey, J., and Thackeray, M. (2004). The significance of the Li_2MnO_3 component in composite $xLi_2MnO_3 \cdot (1-x) LiMn_{0.5}Ni_{0.5}O_2$ electrodes. Electrochem. Commun. 6, 1085–1091.

Kang, S.H., Kempgens, P., Greenbaum, S., Kropf, A., Amine, K., and Thackeray, M. (2007). Interpreting the structural and electrochemical complexity of 0.5 Li_2MnO_3 $0.5LiMO_2$ electrodes for lithium batteries (M = $Mn_{0.5-x}Ni_{0.5-x}Co_{2x}$, $0 \leq x \leq 0.5$). J. Mater. Chem. 17, 2069–2077.

Klein, A., Axmann, P., Yada, C., and Wohlfahrt-Mehrens, M. (2015). Improving the cycling stability of Li_2MnO_3 by surface treatment. J. Power Sources 288, 302–307.

Ko, D.S., Park, J.H., Park, S., Ham, Y.N., Ahn, S.J., Park, J.H., Han, H.N., Lee, E., Jeon, W.S., and Jung, C. (2019). Microstructural visualization of compositional changes induced by transition metal dissolution in Ni-rich layered cathode materials by high-resolution particle analysis. Nano Energy 56, 434–442.

Kondrakov, A.O., Schmidt, A., Xu, J., Geßwein, H., Monig, R., Hartmann, P., Sommer, H., Brezesinski, T., and Janek, J. (2017). Anisotropic lattice strain and mechanical degradation of high-and low-nickel NCM cathode materials for Li-ion batteries. J. Phys. Chem. C 121, 3286–3294.

Kuppan, S., Xu, Y., Liu, Y., and Chen, G. (2017). Phase transformation mechanism in lithium manganese nickel oxide revealed by single-crystal hard X-ray microscopy. Nat. Commun. 8, 14309.

Lee, E.J., Chen, Z., Noh, H.J., Nam, S.C., Kang, S., Kim, D.H., Amine, K., and Sun, Y.K. (2014). Development of microstrain in aged lithium transition metal oxides. Nano Lett. 14, 4873–4880.

Li, Y., Bettge, M., Polzin, B., Zhu, Y., Balasubramanian, M., and Abraham, D. (2013). Understanding long-term cycling performance of $Li_{1.2}Ni_{0.15}Mn_{0.55}Co_{0.1}O_2$–graphite lithium-ion cells. J. Electrochem. Soc. 160, A3006–A3019.

Lim, J.H., Bang, H., Lee, K.S., Amine, K., and Sun, Y.K. (2009). Electrochemical characterization of Li_2MnO_3–$Li[Ni_{1/3}Co_{1/3}Mn_{1/3}]O_2$–$LiNiO_2$ cathode synthesized via co-precipitation for lithium secondary batteries. J. Power Sources 189, 571–575.

Lin, F., Markus, I.M., Nordlund, D., Weng, T.C., Asta, M.D., Xin, H.L., and Doeff, M.M. (2014). Surface reconstruction and chemical evolution of stoichiometric layered cathode materials for lithium-ion batteries. Nat. Commun. 5, 3529.

Liu, Y., Zheng, S., Wang, Q., Fu, Y., Wan, H., Dou, A., Battaglia, V.S., and Su, M. (2017). Improvement of the electrochemical performance of Cr doped layered-spinel composite cathode material $Li_{1.1}Ni_{0.235}Mn_{0.735}Cr_{0.03}O_{2.3}$ with $Li_4Ti_5O_{12}$ coating. Ceram. Int. 43, 8800–8808.

Lu, Z., and Dahn, J.R. (2002). Understanding the anomalous capacity of Li/Li $[Ni_xLi_{(1/3-2X/3)}Mn_{(2/3-X/3)}]O_2$ cells using in situ X-ray diffraction and electrochemical studies. J. Electrochem. Soc. 149, A815–A822.

Mohanty, D., Kalnaus, S., Meisner, R.A., Rhodes, K.J., Li, J., Payzant, E.A., Wood, D.L., and Daniel, C. (2013). Structural transformation of a lithium-rich $Li_{1.2}Co_{0.1}Mn_{0.55}Ni_{0.15}O_2$ cathode during high voltage cycling resolved by in situ X-ray diffraction. J. Power Sources 229, 239–248.

Mohanty, D., Li, J., Abraham, D.P., Huq, A., Payzant, E.A., Wood, D.L., III, and Daniel, C. (2014). Unraveling the voltage-fade mechanism in high-energy-density lithium-ion batteries: origin of the tetrahedral cations for spinel conversion. Chem. Mater. 26, 6272–6280.

Mu, L., Lin, R., Xu, R., Han, L., Xia, S., Sokaras, D., Steiner, J.D., Weng, T.C., Nordlund, D., Doeff, M.M., et al. (2018). Oxygen release induced chemomechanical breakdown of layered cathode materials. Nano Lett. 18, 3241–3249.

Mukhopadhyay, A., and Sheldon, B.W. (2014). Deformation and stress in electrode materials for Li-ion batteries. Prog. Mater. Sci. 63, 58–116.

Odstrčil, M., Menzel, A., and Guizar-Sicairos, M. (2018). Iterative least-squares solver for generalized maximum-likelihood ptychography. Opt. Express 26, 3108–3123.

Pimenta, V., Sathiya, M., Batuk, D., Abakumov, A.M., Giaume, D., Cassaignon, S., Larcher, D., and Tarascon, J.M. (2017). Synthesis of Li-rich NMC: a comprehensive study. Chem. Mater. 29, 9923–9936.

Rodenburg, J., Hurst, A., Cullis, A., Dobson, B., Pfeiffer, F., Bunk, O., David, C., Jefimovs, K., and Johnson, I. (2007). Hard-X-ray lensless imaging of extended objects. Phys. Rev. Lett. 98, 034801.

Rozier, P., and Tarascon, J.M. (2015). Review—Li-rich layered oxide cathodes for next-generation Li-ion batteries: chances and challenges. J. Electrochem. Soc. 162, A2490–A2499.

Ryu, H.H., Park, K.J., Yoon, C.S., and Sun, Y.K. (2018). Capacity fading of Ni-rich Li $[Ni_xCo_yMn_{1-x-y}]$ O_2 $(0.6 \leq x \leq 0.95)$ cathodes for high-energy-density lithium-ion batteries: bulk or surface degradation? Chem. Mater. 30, 1155–1163.

Sasakawa, T., Harada, Y., Takami, N., Kitamura, N., and Idemoto, Y. (2015). Influence of initial charge condition on structural stability and electrochemical properties of $Li_{1.2}Ni_{0.2}Mn_{0.6}O_2$ cathode materials. Electrochim. Acta 174, 406–410.

Schipper, F., Erickson, E.M., Erk, C., Shin, J.Y., Chesneau, F.F., and Aurbach, D. (2017). Review–recent advances and remaining challenges for lithium ion battery cathodes. J. Electrochem. Soc. 164, A6220–A6228.

Strehle, B., Kleiner, K., Jung, R., Chesneau, F., Mendez, M., Gasteiger, H.A., and Piana, M. (2017). The role of oxygen release from Li- and Mn-rich layered oxides during the first cycles investigated by on-line electrochemical mass spectrometry. J. Electrochem. Soc. 164, A400–A406.

Sun, H.H., and Manthiram, A. (2017). Impact of microcrack generation and surface degradation on a nickel-rich layered Li $[Ni_{0.9}Co_{0.05}Mn_{0.05}]O_2$ cathode for lithium-ion batteries. Chem. Mater. 29, 8486–8493.

Tan, S., Ji, Y.J., Zhang, Z.R., and Yang, Y. (2014). Recent progress in research on high-voltage electrolytes for lithium-ion batteries. ChemPhysChem 15, 1956–1969.

Tasaki, K., Goldberg, A., Lian, J.J., Walker, M., Timmons, A., and Harris, S.J. (2009). Solubility of

lithium salts formed on the lithium-ion battery negative electrode surface in organic solvents. J. Electrochem. Soc. *156*, A1019–A1027.

Thackeray, M.M., Kang, S.H., Johnson, C.S., Vaughey, J.T., Benedek, R., and Hackney, S.A. (2007). Li_2MnO_3-stabilized $LiMO_2$ (M = Mn, Ni, Co) electrodes for lithium-ion batteries. J. Mater. Chem. *17*, 3112.

Tran, N., Croguennec, L., Labrugere, C., Jordy, C., Biensan, P., and Delmas, C. (2006). Layered $Li_{1+x}(Ni_{0.425}Mn_{0.425}Co_{0.15})_{1-x}O_2$ positive electrode materials for lithium-ion batteries. J. Electrochem. Soc. *153*, A261.

Tran, N., Croguennec, L., Ménétrerier, M., Weill, F., Biensan, P., Jordy, C., and Delmas, C. (2008). Mechanisms associated with the "plateau" observed at high voltage for the overlithiated $Li_{1.12}(Ni_{0.425}Mn_{0.425}Co_{0.15})_{0.88}O_2$ system. Chem. Mater. *20*, 4815–4825.

Van Heel, M., and Schatz, M. (2005). Fourier shell correlation threshold criteria. J. Struct. Biol. *151*, 250–262.

Wang, J., He, X., Paillard, E., Laszczynski, N., Li, J., and Passerini, S. (2016). Lithium- and manganese-rich oxide cathode materials for high-energy lithium ion batteries. Adv. Energy Mater. *6*, 1600906.

Watanabe, S., Kinoshita, M., Hosokawa, T., Morigaki, K., and Nakura, K. (2014). Capacity fade of $LiAl_yNi_{1-x-y}Co_xO_2$ cathode for lithium-ion batteries during accelerated calendar and cycle life tests (surface analysis of $LiAl_yNi_{1-x-y}Co_xO_2$ cathode after cycle tests in restricted depth of discharge ranges). J. Power Sources *258*, 210–217.

Yan, P., Zheng, J., Gu, M., Xiao, J., Zhang, J.G., and Wang, C.M. (2017). Intragranular cracking as a critical barrier for high-voltage usage of layer-structured cathode for lithium-ion batteries. Nat. Commun. *8*, 14101.

Yang, F., Liu, Y., Martha, S.K., Wu, Z., Andrews, J.C., Ice, G.E., Pianetta, P., and Nanda, J. (2014). Nanoscale morphological and chemical changes of high voltage lithium–manganese rich NMC composite cathodes with cycling. Nano Lett. *14*, 4334–4341.

Yoon, W.S., Chung, K.Y., McBreen, J., and Yang, X.Q. (2006). A comparative study on structural changes of $LiCo_{1/3}Ni_{1/3}Mn_{1/3}O_2$ and $LiNi_{0.8}Co_{0.15}Al_{0.05}O_2$ during first charge using in situ XRD. Electrochem. Commun. *8*, 1257–1262.

Zhan, C., Wu, T., Lu, J., and Amine, K. (2018). Dissolution, migration, and deposition of transition metal ions in Li-ion batteries exemplified by Mn-based cathodes–a critical review. Energy Environ. Sci. *11*, 243–257.

Supplemental Information

Correlated X-Ray 3D Ptychography

and Diffraction Microscopy Visualize

Links between Morphology and Crystal Structure of Lithium-Rich Cath-

ode Materials

Esther H.R. Tsai, Juliette Billaud, Dario F. Sanchez, Johannes Ihli, Michal Odstrčil, Mirko Holler, Daniel Grolimund, Claire Villevieille, and Manuel Guizar-Sicairos

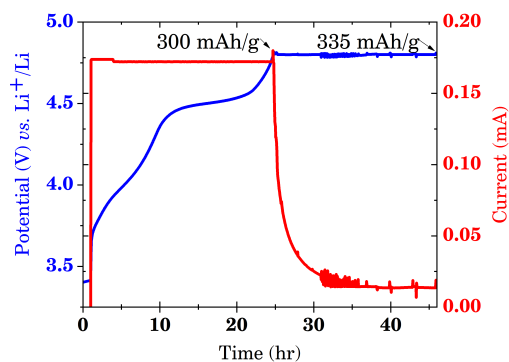# Supplemental Information

---

Supplemental Figures

Figure S1: Evolution of the potential and current as a function of time during the first cycle activation performed at C/20 up to 4.8 V *vs.* Li$^+$/L, related to Fig. 1. After the galvanostatic step, 300 mAh/g are extracted and, after the potentiostatic step, 35 mAh/g are further extracted.
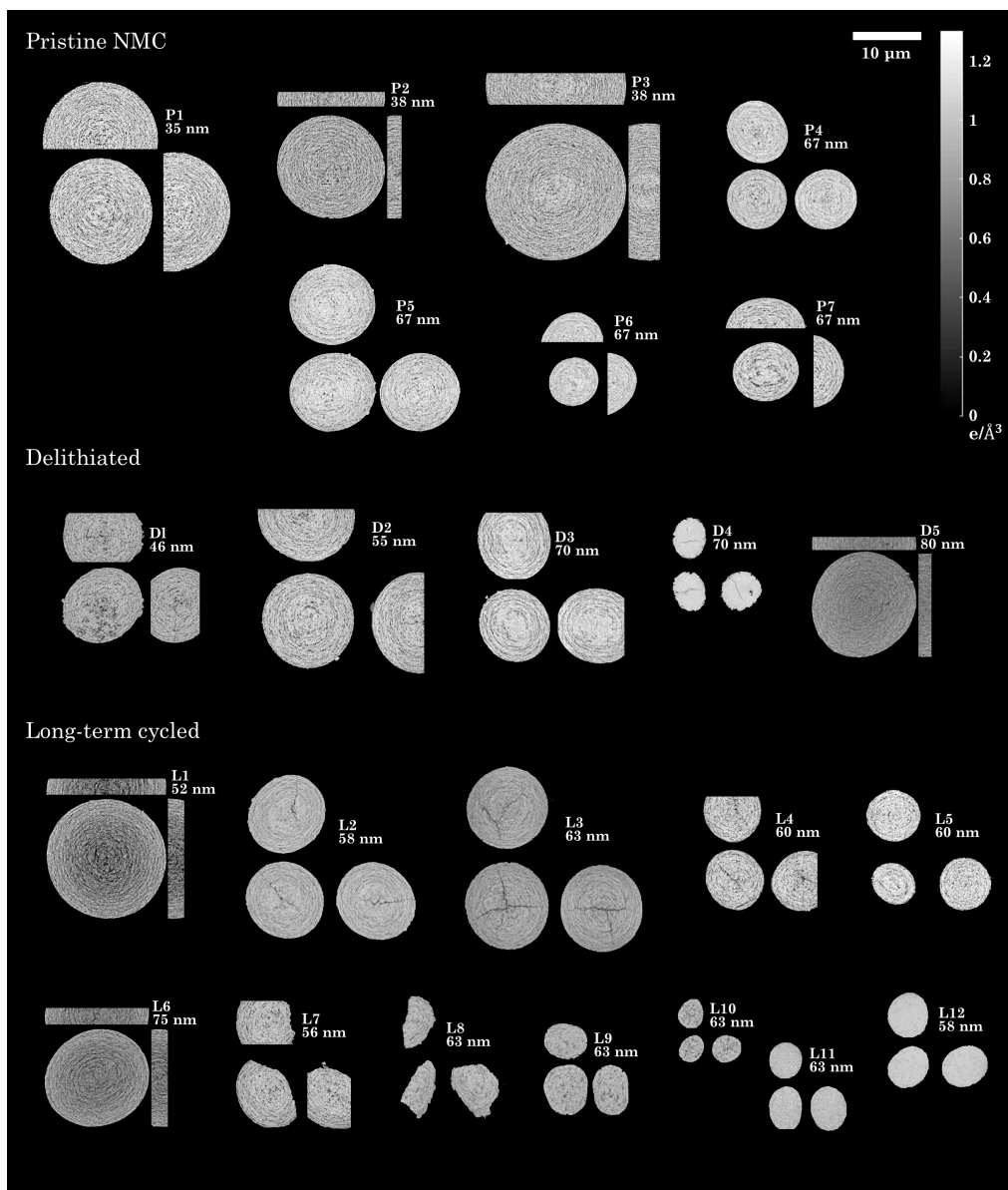
Figure S2: Cross-sections of the electron density tomograms of each particle with 3D resolution labeled, related to Fig. 2. Scale bar 10 μm.
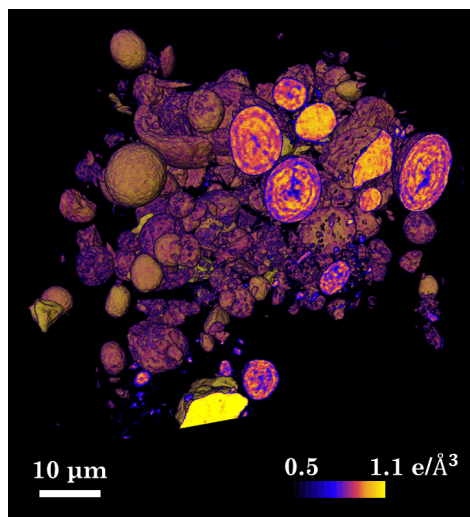
2

Figure S3: Cross-section of the tomogram of delithiated particles using near-field ptychography, giving a 3D resolution of 160 nm. Multiple particles with cracks can be seen, related to Fig. 2.
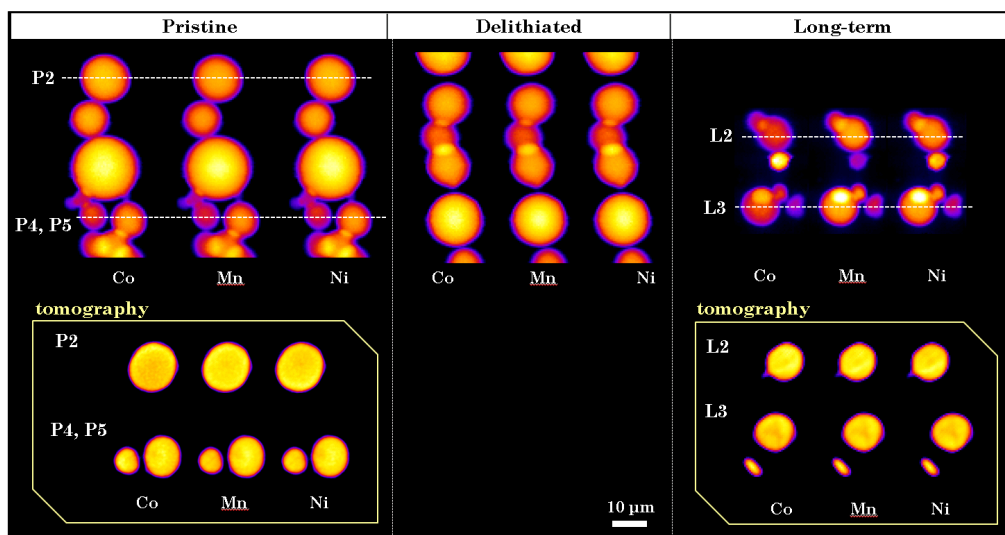

Figure S4: X-ray fluorescence (XRF) projection and corresponding tomography slices, showing homogeneous spatial distributions of transition metals, *i.e.* Co, Mn, and Ni, related to Fig. 4.
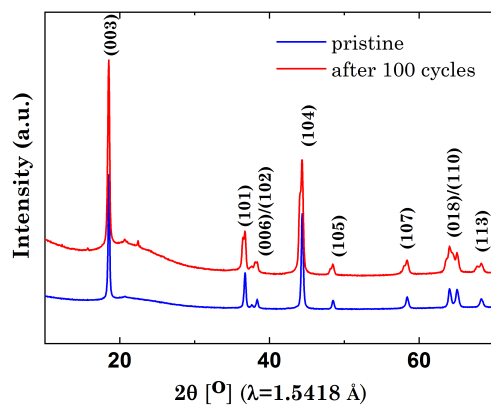
Figure S5: Example of typical X-ray diffractograms of bulk pristine NMC particles and after 100 cycles, related to Fig. 5.

Transparent Methods

Sample preparation and battery testing:

State-of-the-art lithium-rich nickel, manganese, and cobalt oxides were used for the following experiments. The powder electrodes are composed of Li-rich NMC particles and Super C carbon black in a wt% ratio of 90:10, with a loading of 10-15 mg active material. Half cells were assembled using 500 μl LP30 (1M LiPF$_6$ in a 1:1 vol. EC:DMC ratio, BASF) as electrolyte, Li metal (Alfa Aesar) as counter electrode and a glass fibre separator. We used powder as received from the commercial source. The size distribution of the secondary particles allowed for the experiment to be realistic and reliable electrochemical data were obtained. The first charge was performed under galvanostatic cycling conditions at a constant rate of C/20 such as one charge is performed in 20 hours up to 4.8 V *vs.* Li$^+$/Li followed by a potentiostatic step of 24 hours until the current has reached a stable value or close to 0 mA, as seen in Fig. S5. The long term cycling program consisted of the first cycle previously described followed by galvanostatic cycling at a constant rate of C/10 between 2.5 V and 4.8 V *vs.* Li$^+$/Li. Once cycled, the powders were extracted from the cells and washed with DMC, prior to drying. The obtained cycled Li-rich NMC particles were next transferred into tapered glass capillaries, sealed with UV glue, and mounted onto custom-made tomography pins (Holler et al., 2017). The entire preparation procedure was carried out in an Argon-filled glove-box to prevent oxidation and moisturization of the particles.

Electron Microscopy:

Scanning electron micrographs (SEM) were acquired with a Carl Zeiss UltraTM 55 (Germany) apparatus operated at 3 kV accelerating voltage.

Scanning micro- X-ray Diffraction and Fluorescence:

Scanning X-ray diffraction (XRD) and X-ray fluorescence (XRF) data were collected at the microXAS beamline (X05LA), Swiss Light Source (SLS), Paul Scherrer Institut, Switzerland. A 17.3 keV incident pencil beam was focused using a Kirkpatrick-Baez (KB) mirror system to a size of 1 μm^2. Li-rich NMC particles in capillaries mounted on tomography pins (Holler et al., 2017) were raster-scanned in projection mode with a step size of 0.5 μm, and in scanning tomography mode with a lateral step size of 0.5 μm at several projections equally spaced by around 1° over 180°. Diffraction patterns were

recorded using a DECTRIS Eiger 4M detector. XRF spectra were collected simultaneously by two silicon drift detectors (SDD) positioned in opposite sides at a perpendicular angle with respect to the incoming pencil beam. The acquisition of time 0.3 seconds per point was used for both XRD and XRF data. Al_2O_3 polycrystals were used to calibrate the sample to XRD detector geometry. XRDUA was used for the radial integration of the individual 2D diffraction patterns and for the modelling of the 1D powder diffraction patterns (De Nolf et al., 2014). The tomographic reconstructions were carried out using in-house developed Python routines based on the ASTRA library (Aarle et al., 2015). For each voxel, a full 1D powder XRD pattern is retrieved.

Ptychographic X-ray Computed Tomography:

Ptychographic X-ray computed tomography (PXCT) experiments were performed at the cSAXS beamline (X12SA), SLS, Paul Scherrer Institut, Switzerland. Two variants of PXCT were utilized in this work. Near-field ptychographic tomography was used to obtain tomograms of large field of view at reduced spatial resolution to provide a more robust overview of the sample population (Stockmar et al., 2015; Stockmar et al.). On the other hand, far-field measurements provide reconstructions at higher resolution but conversely smaller field-of-views (FOVs) within similar acquisition time frames. Here we provide a general description of the PXCT experiment for the multiple measurements that were conducted. A double crystal Si(111) monochromator was used to define a monochromatic radiation of around 7 keV. A Fresnel zone plate (FZP) (Gorelick et al., 2011) with an outer-most zone width of 60 nm and a diameter of 150 μm was coherently illuminated by an upstream slit of 20μm horizontal width. A gold central beam stop of 50 μm diameter was placed upstream the FZP and an order sorting aperture with 30 μm diameter was mounted downstream near the focus to block higher orders of diffraction and the undiffracted beam. Both the FZP and the central stop were fabricated in the Laboratory for Micro and Nanotechnology, Paul Scherrer Institut, Switzerland. The sample was placed a few mm downstream of the focus where the illumination was about 5 μm diameter for the far-field ptychography measurements and scanned over a FOV of around 300 μm² following a Fermat spiral pattern (Huang et al., 2014) with a step size of approximately 1 μm, giving roughly 300 scanning points. At each scanning point, a diffraction pattern was recorded around 7.2 m downstream of the object by either a Pilatus 2M detector (Henrich et al., 2009) or an Eiger

detector (Guizar-Sicairos et al., 2014) with a 0.1 s exposure time, giving approximately 2×10^7 photons per diffraction pattern and 3×10^7 photons/μm^2 on the sample. Around 800 projections were taken for each sample, giving a measurement time of approximately 12 hours per sample. A region of the detector frames was cropped for further processing, for which the cropped sizes were chosen to have an object pixel size around 20 nm. A projection-based algorithm was used for its robustness and fast convergence (Thibault et al., 2008), which was followed by a maximum-likelihood refinement to provide the final solution accounting for the noise statistics (Guizar-Sicairos and Fienup, 2008; Thibault and Guizar-Sicairos, 2012). Near-field ptychographic tomography experiments follow the same procedure. A 50 μm illumination and a 10 μm step-size was used to cover a FOV of roughly 5000 μm^2 in 5 hours with 480 projections, giving a resolution of 160 nm. With synchrotron upgrades as well as improved optics and computational power, in the future it is possible to have a throughput that is orders of magnitude higher than the current study (Hettel, 2014; Thibault et al., 2014).

Analysis and segmentation:

Analysis, segmentation, as well as visualization were carried out using in-house developed Matlab routines, Fiji (Schindelin et al.; Arganda-Carreras et al., 2017; Hall et al., 2009), and FEI Avizo. Reconstructed particles were extracted through Avizo and ImageJ for visualization and analysis. Air and glass capillary surrounding the Li-rich NMC particles was removed by interactively thresholding the electron density tomograms and subsequent morphological operations, therewith creating a binary mask. This binary mask was then used as an input for 3D distance maps to calculate the distance from particle core to exterior, allowing radially averaged electron density. Segmentation was done by the training segmentation Weka (Frank et al., 2016; Hall et al., 2009) in ImageJ (Schneider et al., 2012). With Avizo, thickness maps were used to calculate pore diameter maps and derive pore-size distributions (Hildebrand and Rüegsegger, 1997). Due to finite spatial resolution, only pores with diameters slightly larger than the attained spatial resolution were considered.

Aarle, W.V., Palenstijn, W.J., Beenhouwer, J.D., Altantzis, T., Bals, S., Batenburg, K.J., and Sijbers, J. (2015). The ASTRA toolbox: A platform for advanced algorithm development in electron tomography. Ultramicroscopy *157*, 35 – 47.

Arganda-Carreras, I., Kaynig, V., Rueden, C., Eliceiri, K.W., Schindelin, J., Cardona, A., and Sebastian Seung, H. (2017). Trainable Weka segmentation: a machine learning tool for microscopy pixel classification. Bioinformatics *33*, 2424–2426.

De Nolf, W., Vanmeert, F., and Janssens, K. (2014). XRDUA: crystalline phase distribution maps by two-dimensional scanning and tomographic (micro) X-ray powder diffraction. J. Appl. Crystallogr. *47*, 1107–1117.

Frank, E., Hall, M.A., and Witten, I.H. (2016). The WEKA workbench. online appendix for "data mining: Practical machine learning tools and techniques .

Gorelick, S., Vila-Comamala, J., Guzenko, V.A., Barrett, R., Salomé, M., and David, C. (2011). High-efficiency Fresnel zone plates for hard X-rays by 100 keV e-beam lithography and electroplating. J. Synchrotron Radiat. *18*, 442–446.

Guizar-Sicairos, M., and Fienup, J.R. (2008). Phase retrieval with transverse translation diversity: a nonlinear optimization approach. Opt. Express *16*, 7264–7278.

Guizar-Sicairos, M., Johnson, I., Diaz, A., Holler, M., Karvinen, P., Stadler, H.C., Dinapoli, R., Bunk, O., and Menzel, A. (2014). High-throughput ptychography using eiger: scanning x-ray nano-imaging of extended regions. Opt. Express *22*, 14859–14870.

Hall, M., Frank, E., Holmes, G., Pfahringer, B., Reutemann, P., and Witten, I.H. (2009). The WEKA data mining software: An update. SIGKDD explorations *11*.

Henrich, B., Bergamaschi, A., Broennimann, C., Dinapoli, R., Eikenberry, E.F., Johnson, I., Kobas, M., Kraft, P., Mozzanica, A., and Schmitt, B. (2009). Pilatus: A single photon counting pixel detector for x-ray applications. Nucl. Instrum. Methods Phys. Res. A *607*, 247–249.

Hettel, R. (2014). DLSR design and plans: an international overview. J. Synchrotron Radiat. *21*, 843–855.

Hildebrand, T., and Rüegsegger, P. (1997). A new method for the model-independent assessment of thickness in three-dimensional images. J. Microsc. *185*, 67–75.

Holler, M., Raabe, J., Wepf, R., Shahmoradian, S.H., Diaz, A., Sarafimov, B., Lachat, T., Walther, H., and Vitins, M. (2017). OMNY PIN-A versatile sample holder for tomographic measurements at room and cryogenic temperatures. Rev. Sci. Instrum. *88*, 113701.

Huang, X., Yan, H., Harder, R., Hwu, Y., Robinson, I.K., and Chu, Y.S. (2014). Optimization of overlap uniformness for ptychography. Opt. Express *22*, 12634–12644.

Schindelin, J., Arganda-Carreras, I., Frise, E., Kaynig, V., Longair, M., Pietzsch, T., Preibisch, S., Rueden, C., Saalfeld, S., and Schmid, B.Fiji: an open-source platform for biological-image analysis .

Schneider, C.A., Rasband, W.S., and Eliceiri, K.W. (2012). NIH image to ImageJ: 25 years of image analysis. Nature Methods *9*, 671–675.

Stockmar, M., Hubert, M., Dierolf, M., Enders, B., Clare, R., Allner, S., Fehringer, A., Zanette, I., Villanova, J., and Laurencin, J.X-ray nanotomography using near-field ptychography .

Stockmar, M., Zanette, I., Dierolf, M., Enders, B., Clare, R., Pfeiffer, F., Cloetens, P., Bonnin, A., and Thibault, P. (2015). X-ray near-field ptychography for optically thick specimens. Phys. Rev. Appl. *3*, 014005.

Thibault, P., Dierolf, M., Menzel, A., Bunk, O., David, C., and Pfeiffer, F. (2008). High-resolution scanning x-ray diffraction microscopy. Science *321*, 379–382.

Thibault, P., and Guizar-Sicairos, M. (2012). Maximum-likelihood refinement for coherent diffractive imaging. New J. Phys. *14*, 063004.

Thibault, P., Guizar-Sicairos, M., and Menzel, A. (2014). Coherent imaging at the diffraction limit. J. Synchrotron Radiat. *21*, 1011–1018.